



PCCP

Extracting multivalent detachment rates from heterogeneous nanoparticle populations

Journal:	<i>Physical Chemistry Chemical Physics</i>
Manuscript ID	CP-ART-05-2018-003118.R2
Article Type:	Paper
Date Submitted by the Author:	19-Jul-2018
Complete List of Authors:	Wang, Mingqiu; University of California Irvine, Biomedical Engineering Allard, Jun; University of California Irvine, MATH Haun, Jered; University of California Irvine, Biomedical Engineering

SCHOLARONE™
Manuscripts

Extracting multivalent detachment rates from heterogeneous nanoparticle populationsMingqiu Wang,¹ Jun Allard,^{3,4,6} and Jered B. Haun^{1,2,5,*}¹ Department of Biomedical Engineering, University of California Irvine, Irvine, CA 92697² Department of Chemical Engineering and Materials Science, University of California Irvine, Irvine, CA 92697³ Department of Mathematics, University of California Irvine, Irvine, CA 92697⁴ Department of Physics and Astronomy, University of California Irvine, Irvine, CA 92697⁵ Chao Family Comprehensive Cancer Center, University of California Irvine, Irvine, CA 92697⁶ Center for Complex Biological Systems, University of California Irvine, Irvine, CA 92697

*Jered B. Haun, PhD

Department of Biomedical Engineering, University of California Irvine

3107 Natural Sciences II, Irvine, CA, 92697

Phone: 949-824-1243

E-mail: jered.haun@uci.eduHomepage: <http://haun.eng.uci.edu>**keywords:** nanoparticle, multivalent adhesion, detachment kinetics, simulation, Nano Adhesive Dynamics, targeting

Abstract

Nanoparticles can form multiple bonds with target surfaces, thereby increasing adhesion strength and internalization rate into cells. This property has helped to drive interest in nanoparticles as delivery vehicles for drugs and imaging agents, but significant gaps in our understanding of multivalent adhesion make it difficult to control and optimize binding dynamics. In previous work, we experimentally observed that multivalent nanoparticle adhesion can exhibit a time-dependent detachment rate. However, simulations later indicated that the underlying cause was variability in the number of bonds that form for individual nanoparticles within the population. Here, we use this insight to develop a simple model to isolate a series of constant detachment rates for heterogeneous populations. Using simulations of experimental data to train the model, we first classified nanoparticles within a given population based on the most likely equilibrium bond number, which we termed the bond potential. We then assumed that each bond potential category would follow standard first-order kinetics with constant detachment rates. Model results matched the population binding data, but only if we further divided each bond potential category into two sub-components, the second of which did not detach. We then utilized bonding rates from the simulation to estimate detachment rates for the second, slower detaching sub-component. These results confirm our hypothesis that nanoparticle populations can be sub-divided based on bond potential, each of which could be characterized by a constant detachment rate. Finally, we established relationships between the new heterogeneous population detachment model and a time-dependent, empirical detachment model that we developed in previous work. This could make it possible to determine bond potential distributions directly from experimental data without computationally costly simulations, which will be explored in future work.

Introduction

A major attribute of nanoparticles (NPs) is the ability to form multiple bonds, which improves adhesion strength and cell internalization rate.^{1–10} However, our current understanding of multivalent NP binding has been limited by a lack of insight into key details such as bonding dynamics and equilibrium number. A major challenge is that experimental systems cannot assess individual bonds, and thus interpretations must be made based on macroscopic NP behavior. Another issue is that the location of affinity molecules on NPs and target surfaces are random, and thus the number of bonds that form can vary substantially amongst the individual NPs within an ensemble. NP adhesion is typically characterized at the population scale, using a single metric such as the observed equilibrium affinity constant, or avidity. If bonding heterogeneity were significant within a population, then a series of adhesion parameters should be obtained that correspond to the relevant bond numbers. This is similar in concept to theoretical works that sought to partition a multivalent binding population into discrete bond valency states that were each attributed a unique thermodynamic free energy.^{11–16} However, determining accurate free energy or kinetic rate parameters for each bond state is a major challenge.

Previously, we assessed multivalent NP adhesion using flow chamber assays, and determined the rates of attachment (k_A) and detachment (k_D) using a simple kinetic model.^{3,5,8} We found that k_D was complex, appearing to decrease over time following an empirical power law with magnitude (k_D^0) and temporal (β) parameters. In subsequent work, we developed a multi-scale, biophysical simulation called Nano Adhesive Dynamics (NAD) to further investigate the time-dependent detachment phenomenon.¹⁷ NAD simulations contained elements from previous Adhesive Dynamics works modeling leukocytes, platelets, and viruses,^{18–23} including transport via fluid flow and Brownian motion, mechanical forces, and bonding properties. NAD simulations recapitulated experimental binding data, including time-dependent detachment behavior with correct β and k_D^0 values. We concluded that long-term, minute-scale changes in

NP detachment rate were directly caused by NP bonding heterogeneity. Over time, NPs restricted to low bond numbers were preferentially eliminated by detachment, evolving the remaining NP population towards higher adhesion stability. This demonstrated that a population of NPs cannot be represented by a single multivalent detachment rate, and for that matter, affinity/avidity. Instead, a series of detachment rates co-exist together, each corresponding to sub-populations with different bond numbers.

Here, we develop a simple approach to determine multivalent NP detachment rates for populations exhibiting significant bonding heterogeneity. The foundational hypothesis is that appropriately classifying the population based on a metric of bonding ability, the detachment of each sub-population will follow standard first-order kinetics characterized by a constant detachment rate. Using NAD simulations of experimental data, we show that mode bond number provides a good initial classification criterion, which we call the bond potential (BP). However, we still observe non-first-order kinetics within some BP categories. We address this issue by assuming that each BP can contain two sub-components, one that detaches and one that does not detach during the time-scale that was observed. We then determine non-zero detachment rates for slow detaching sub-components from bond formation and rupture rates using a simple bond state model and mean first passage time estimates. From these results, we conclude that secondary sub-components within BPs are actually rare, and detachment rates only vary substantially if single bond chemical or mechanical properties are varied, as valency effects are already captured by BP sub-categorization. Finally, we employ a survival analysis to establish relationships between the parameters of the new heterogeneous population detachment model and the time-dependent, empirical model from previous work.

Methods

Adhesion Dynamics (NAD) Simulations. For this work, we investigated a NP adhesion system that we studied in our previous experimental work.³ This included a 210 nm polystyrene

sphere that was coated with a monoclonal antibody and a glass slide that was coated with ICAM-1 protein. Specifically, we employed ICAM-1 at low ($21 \mu\text{m}^{-2}$) and medium ($41 \mu\text{m}^{-2}$) coating densities, as well as anti-ICAM-1 antibody at low ($410 \mu\text{m}^{-2}$ or 28/NP) and medium ($1080 \mu\text{m}^{-2}$ or 75/NP) coating densities. NAD simulations were performed in previous work to match experimental data.¹⁷ Bond properties were as follows: intrinsic formation rate (k_f^0) = $1.5 \times 10^5 \text{ s}^{-1}$, intrinsic rupture rate (k_r^0) = $1.1 \times 10^{-4} \text{ s}^{-1}$, spring constant (σ) = 0.8 N/m, and reactive compliance (γ) = 0.274 nm, and ICAM-1 was presented in three different configurations: monomers, dimers, and clustered dimers. In addition to these published experimental and simulation results, we also performed new NAD simulations in which bond stability was decreased so that NP detachment would be observed at higher bond numbers. These new simulations all employed the medium antibody density, medium ICAM-1 density, ICAM-1 arranged as monomers, and the bond properties listed above with one of the following modifications: $\gamma = 0.29 \text{ nm}$, $\gamma = 0.3 \text{ nm}$, $k_r^0 = 5 \times 10^{-4} \text{ s}^{-1}$, or $k_r^0 = 1.1 \times 10^{-3} \text{ s}^{-1}$.

Empirical Detachment Model. In previous work, we modeled NP detachment in a similar manner to classic kinetic treatments of monovalent bonding. Specifically, we sought to determine a detachment rate (k_D) for the NP ensemble that is observed after initial tethering to a surface, as follows:

$$\frac{\partial B}{\partial t} = -k_D(t)B \quad 1.$$

where B is the number of bound NPs and t is time. We observed that k_D decreased over time, which was captured using an empirical power law:

$$k_D(t) = \frac{k_D^0}{(t/t_{ref})^\beta} \quad 2.$$

where k_D^0 and β are magnitude and temporal parameters, respectively, and t_{ref} is a reference time. Substituting eq 1 into eq 2 and integrating yields:

$$\frac{B}{B^0} = \exp\left(\frac{k_D^0 t^{1-\beta}}{t_{ref}^\beta \beta - 1}\right) \quad 3.$$

where B^0 is the initial number of NPs bound. Note that we originally treated t_{ref} as a variable of convenience to maintain unit consistency.³ However, we later found from NAD simulations that the steady state for multivalent bond formation was achieved at approximately 0.1 s.¹⁷ Thus, we used $t_{ref} = 0.1$ s for this work, and if necessary re-fit previously reported experimental and simulation results.^{3,17}

Classification of NPs into Bond Potentials. The stochastic distribution of adhesion molecules on the NP and substrate lead to variations bond number within a given NP population. We previously developed the term bond potential (BP) to characterize this phenomenon. For this work, we chose to define BP based on the mode bond number observed in NAD simulations. We assume that NPs within the same BP category generally share the same adhesion properties, including kinetic rates and thermodynamic energy. However, we do note that this is a broad categorization, and thus variability may still exist. For example, a less favorable orientation of the same number of bonds could lead to higher bond strain and rupture rate. We will account for to this possibility by allowing for the presence of hidden sub-components within each BP. We believe that this approach is more intuitive than defining BPs with non-integer values, as bond number will be a whole number at any given time. The hidden sub-components further divide BPs with respect to adhesion properties.

Detachment Model for Heterogeneous Populations. Within each BP category, we hypothesized that detachment will follow eq 1, but now with to a constant k_D value unique to that BP category, as follows:

$$\frac{\partial B_i}{\partial t} = -k_{D,i} B_i \quad 4.$$

where i designates the BP and $k_{D,i}$ is the detachment rate for BP i . Integrating eq 4 yields:

$$B_i(t) = B_i^0 e^{-k_{D,i}t} \quad 5.$$

Thus, each BP will follow first-order kinetics and can be fit using a simple exponential decay.

The complex, apparently time-dependent detachment profile for the entire population can then be recreated by summing the results for each BP:

$$B(t) = \sum_{i=1}^m B_i(t) = \sum_{i=1}^m B_i^0 e^{-k_{D,i}t} \quad 6.$$

$$B^0 = \sum_{i=1}^m B_i^0$$

where B_i^0 is the initial number of NPs in BP i and m is the maximum BP observed for the population.

For BPs with hidden sub-components, eq 5 can be generalized to include terms for each sub-component as follows:

$$B_i(t) = B_i^0 \sum_{j=1}^k \alpha_i^{(j)} e^{-k_{D,i}^{(j)}t} \quad 7.$$

$$1 = \sum_{j=1}^k \alpha_i^{(j)}$$

where j designates sub-component number, $\alpha_i^{(j)}$ is the relative number of BP i NPs in component j , $k_{D,i}^{(j)}$ is the detachment rate for BP i NPs in sub-component j , and k is the total number of sub-components. As described in the results section, we found that NAD simulation data was well characterized using two sub-components, one of which did not detach at all. This simplifies eq 7 to:

$$\frac{B_i}{B_i^0} = \alpha_i e^{-k_{D,i}t} + (1 - \alpha_i) \quad 8.$$

Determining formation and rupture rates for all bond state transitions. A limitation of the previous section is that we can only determine detachment rates for BPs and/or sub-components that actually detached over the time-scale observed. We postulated that detachment rates for the non-detaching NP sub-populations could be determined from bonding information that is also available in NAD simulations. Thus, bond formation and rupture rates for all bond state transitions were determined by tracking instantaneous bond numbers for each BP category. We defined the relative number of NPs in BP i with bond number j as $S_{i,j}$. At any given time, the number of NPs in each BP category must also be equal to the sum of all bond number states:

$$\frac{B_i(t)}{B_i^0} = \sum_{j=1}^N S_{i,j}(t) \quad 9.$$

where N is maximum bond number. We further defined $S_{i,j}$ based on the rates of bond formation (k_f) and rupture (k_r) for all state transitions, as dictated by the following master equation:

$$\begin{aligned} \frac{dS_{i,j}}{dt} &= -k_{r,i,j}S_{i,j} - k_{f,i,j+1}S_{i,j} + k_{r,i,j+1}S_{i,j+1} + k_{f,i,j}S_{i,j-1} \\ \frac{dS_{i,d}}{dt} &= k_{diff}S_{i,0} \end{aligned} \quad 10.$$

or:

$$\frac{d\mathbf{S}_i}{dt} = \mathbf{K}_i\mathbf{S}_i$$

where \mathbf{K}_i is the transition matrix for BP i and \mathbf{S}_i is a vector of all bond states ($S_{i,j}$). Further description of \mathbf{K}_i and \mathbf{S}_i are included in the Supplementary Information Methods. The terms $S_{i,d}$ and k_{diff} were included to account for the fact that NP tracking experiments cannot detect detachment until after a NP with zero bonds has translated from the attachment site. If we allow for two sub-components within each BP, the master equation (eq 10) can be modified as follows:

$$\begin{aligned}
\frac{dS_{i,j}^{(1)}}{dt} &= P_{f,i,j}(k_{f,i,j}^{(1)}S_{i,j-1}^{(1)} + k_{f,i,j}^{(2)}S_{i,j-1}^{(2)}) \\
&+ P_{r,i,j+1}(k_{r,i,j+1}^{(1)}S_{i,j+1}^{(1)} + k_{r,i,j+1}^{(2)}S_{i,j+1}^{(2)}) \\
&\quad - k_{r,i,j}^{(1)}S_{i,j}^{(1)} \\
&\quad - k_{f,i,j+1}^{(1)}S_{i,j}^{(1)} \\
\frac{dS_{i,j}^{(2)}}{dt} &= (1 - P_{f,i,j})(k_{f,i,j}^{(2)}S_{i,j-1}^{(2)} + k_{f,i,j}^{(1)}S_{i,j-1}^{(1)}) \\
&+ P_{r,i,j+1}(k_{r,i,j+1}^{(2)}S_{i,j+1}^{(2)} + k_{r,i,j+1}^{(1)}S_{i,j+1}^{(1)}) \\
&\quad - k_{r,i,j}^{(2)}S_{i,j}^{(2)} \\
&\quad - k_{f,i,j+1}^{(2)}S_{i,j}^{(2)} \\
\frac{dS_{i,d}}{dt} &= k_{diff}(S_{i,0}^{(1)} + S_{i,0}^{(2)})
\end{aligned} \tag{11}$$

or:

$$\frac{d\mathbf{S}_i}{dt} = \mathbf{K}_i\mathbf{S}_i$$

where $S_{i,j}^{(1)}$ and $S_{i,j}^{(2)}$ correspond to hidden components 1 and 2, respectively, $P_{f,i,j}(\in [0,1])$ is the relative number of NPs transitioning from state $j-1$ to j for component 1, and $P_{r,i,j}(\in [0,1])$ is the relative number of NPs transitioning from state j to $j-1$ for component 1. We note that NPs can freely cross between sub-components, which means that the system of NPs does not retain memory. Based on these assumptions, the system of differential equations must be solved simultaneously and components 1 and 2 cannot be interpreted in isolation from each other. Vectorized representations of \mathbf{S}_i and \mathbf{K}_i for use with eq 11 are given in the Supplementary Information Methods.

Since there are a large number of transition rates in eqs 10 and 11, we employed two simplification strategies. First, we determined exact values for $k_{r,1,1}$ and k_{diff} using NAD simulations in which the NP was attached via a single tether, and additional bonds were not allowed to form (see Supplementary Information Methods and Fig. S1). The second

simplification was to estimate the remaining transition rates (k_f and k_r) from the average pause times observed between bond number transitions in full, as described in the Supplementary Information (see Supplementary Information Methods and Fig. S1). The system of ODEs in either eq 10 or 11 were solved simultaneously using the “minimize” function in Python LMFIT library, with $k_{r,1,1}$ and k_{diff} values set as constants, and the pause time k_f and k_r values employed as initial conditions.

Estimating Macroscopic Detachment Rates from Bond Transition Rates. The microscopic bonding rates obtained in the previous section can be used to estimate a macroscopic detachment rate from the transition matrix (\mathbf{K}_i) using the mean first passage time.²⁶ We defined T_{ij} as the first passage time of BP i and bond state j , and \mathbf{T}_i is a vector containing the first passage times for all N bond states. The vector \mathbf{T}_i can be calculated directly from the

$$\mathbf{T}_i = -\mathbf{K}_i^{-1} \mathbf{E}^T \quad 12.$$

transition matrix, as follows:

where \mathbf{E} is a vector with $N+2$ elements that are all equal to unity, and the superscript T refers to a matrix transpose. The elements of vector \mathbf{T}_i can then be averaged to determine the mean first passage time, which in turn can be inverted to obtain a detachment rate as follows:

$$k^{(M)}_{D,i} = N / \sum_{j=0}^N T_{i,j} \quad 13.$$

We employed a unique designation for $k^{(M)}_{D,i}$ because it corresponds to both sub-components of a given BP.

Determining Detachment Rates for Non-detaching Subpopulations. We performed heterogeneous population detachment model fitting again using two sub-components (eq 7), but

now enforcing $k^{(M)}_{D,i}$ as an additional constraint. Specially, we used three fitting parameters: two detachment rates ($k^{(1)}_{D,i}$ and $k^{(2)}_{D,i}$), as well as the first component weight α_i , as follows:

$$B_i(t) = B_i^0 \left[\alpha_i e^{-k^{(1)}_{D,i} t} + (1 - \alpha_i) e^{-k^{(2)}_{D,i} t} \right]$$

such that:

14.

$$k^{(M)}_{D,i} = \frac{\alpha_i}{k^{(1)}_{D,i}} + \frac{1 - \alpha_i}{k^{(2)}_{D,i}}$$

In this manner, we achieved non-zero detachment rates for all sub-components and BPs.

Relating the Heterogenous Population and Empirical Detachment Models. Finally, we sought to establish relationships between the population heterogeneity detachment model developed in the previous section with the empirical detachment model in eq 1. Our approach was to use a classic survival analysis,^{24,25} which describes any irreversible stochastic process by a hazard function. We first defined the general hazard function, $H(t)$, to describe the instantaneous detachment rate, as follows:

$$H(t) = -\frac{1}{B(t)} \frac{dB}{dt} = -\frac{d}{dt} \ln \frac{B(t)}{B^0} \quad 15.$$

We again assumed that each BP can contain two sub-components, and for simplicity assumed that one did not detach over the time-scale observed. Using eqs 7 and 8, we can approximate $B(t)$, denoted as $\tilde{B}(t)$, as follows:

$$\begin{aligned} \frac{\tilde{B}(t)}{B^0} &= (1 - \Sigma_i (1 - \alpha_i) w_i^0) \exp \left[- \left(\sum_i \frac{\alpha_i w_i^0}{k_{D,i}} \right)^{-1} t \right] + \Sigma_i (1 - \alpha_i) w_i^0 \\ &= (1 - \tilde{p}) e^{-\frac{t}{\tilde{\tau}}} + \tilde{p} \end{aligned}$$

where

16.

$$\begin{aligned} \tilde{p} &= \Sigma_i (1 - \alpha_i) w_i^0, \\ \tilde{\tau} &= \left(\sum_i \frac{\alpha_i w_i^0}{k_{D,i}} \right) \end{aligned}$$

and w_i^0 is the initial ratio of NPs in BP i relative to the initial full population (i.e. B_i^0/B^0).

Combining eqs 15 and 16, we can approximate the hazard function as $\tilde{H}(t)$:

$$\tilde{H}(t) = \frac{1}{\tilde{t}} \cdot \frac{1}{1 + \frac{\tilde{p}}{1 - \tilde{p}} e^{t/\tilde{t}}} \quad 17.$$

We can similarly establish a hazard function for the empirical model using eq 2 as $H^*(t)$:

$$H^*(t) = \frac{k_D^0}{(t/t_{ref})^\beta} \quad 18.$$

This implies the following bond survival probability:

$$B^*(t) = \exp\left(-\int_0^t H^*(t') dt'\right) = \exp\left(-\frac{k_D^0 t_{ref}}{1 - \beta} \cdot (t/t_{ref})^{(1-\beta)}\right) \quad 19.$$

Given the two hazard functions, we then imposed equality at two time points. We first chose t_{ref} , the bond steady state. At $t = t_{ref}$, assuming $\tilde{H}(t_{ref}) = H^*(t_{ref})$ implies

$$k_D^0 = \frac{1}{\tilde{t}} \cdot \frac{1}{1 + \frac{\tilde{p}}{1 - \tilde{p}} e^{t_{ref}/\tilde{t}}} \quad 20.$$

We also chose an arbitrary later time defined as t_{max} . At $t = t_{max}$, assuming $\tilde{H}(t_{max}) = H^*(t_{max})$ implies

$$\beta = \frac{\ln\left(\frac{1 + \frac{\tilde{p}}{1 - \tilde{p}} e^{t_{ref}/\tilde{t}}}{1 + \frac{\tilde{p}}{1 - \tilde{p}} e^{t_{max}/\tilde{t}}}\right)}{\ln\left(\frac{t_{ref}}{t_{max}}\right)} \quad 21.$$

where eq 20 was used to substitute for k_D^0 . Eqs 20 and 21 provide approximate relationships between empirical model parameters (k_D^0 and β) and the heterogeneous population model parameters ($k_{D,i}$, w_i^0 , and α_i).

Results

Detachment Model for Heterogeneous Populations

To develop and validate the model, we used experimental and NAD simulation results at medium antibody density ($1080 \mu\text{m}^{-2}$) on the NP and medium ICAM-1 density ($41 \mu\text{m}^{-2}$) on the substrate.^{3,17} NPs were assigned to a BP based on mode bond number, which resulted in six BP categories that were distributed as shown in Fig. 2A. Also indicated in Fig. 2A is the number of NPs that detached by the end of the simulation, which ranged from 100% for BP1 to 0% for BPs 4-6. Detachment profiles for BPs 1-3 are shown separately in Fig. 2B, along with exponential decay fits obtained using eq 5. The fits matched well for BP 1, but deviations for BPs 2 and 3 indicated non-first-order kinetics. We attributed these deviations to bonding heterogeneity still being present even within BP categories. Therefore, we further divided BPs into sub-components, and using eq 7 we found that two sub-components was sufficient to match the simulation data. We also observed that fitting results were similar if we assumed that the second component did not detach at all (i.e. $k_{D,i}^{(2)} = 0$, see Supplementary Information, Fig. S2), as described by eq 8. Detachment rate constants ($k_{D,i}$) and relative fractions (α_i) for sub-component 1 are listed in Table 1. Both $k_{D,i}$ and α_i decreased with BP, indicating greater adhesion stability as we would expect for sub-populations with higher average bond numbers. The detachment data for the full NP population is shown in Fig. 2C, along with the reconstructed profiles obtained for the heterogeneous population detachment model (eq 6) under both one and two sub-component scenarios. The empirical model was also used to fit the simulation data using eq 2. The two-component BP model matched the NAD simulation data best, as the other fits diverged at either short or long times.

Next we followed the same approach using four more parameter conditions, which varied from the base case as follows: lower antibody density ($410 \mu\text{m}^{-2}$), lower ICAM-1 density ($21 \mu\text{m}^{-2}$), arranged of ICAM-1 as dimers, and arrangement of ICAM-1 as clustered dimers of 4 molecules.¹⁷ Bond potential distributions are shown in Figs. 3A-D, and generally shifted to lower

numbers compared to the base case in Fig. 2A. As expected, this shift was associated with higher levels of NP detachment, although most still detached from BPs 1 and 2. Individual detachment fits for each BP can be found for both one (eq 5) and two (eq 8) components in Supplementary Information (see Supplementary Information, Fig. S3). Full population fits using the heterogeneous population detachment model with one and two sub-components, as well as the empirical detachment model (eq 2) are given in Figs. 3E-H. Two component BP model fits again matched simulation data best across all conditions. Detachment rate constants ($k_{D,i}$) and relative fractions (α_i) for sub-component 1 of each BP are listed in Table 1. The most notable differences relative to the base case were in $k_{D,1}$, which increased for all but one condition (lower ICAM-1 density).

Our next goal was to explore detachment from higher BPs, and therefore we performed new NAD simulations using the base case under less stable single bond conditions γ (0.29 and 0.3 nm) or k_r^0 (5×10^{-4} and 10^{-3} s^{-1}). BP distributions are shown in Figs. 4A-D, and were similar to the base case in Fig. 2A. This suggests that final bond numbers were dictated primarily by adhesion molecule availabilities, not single bond properties. Instead, lower individual bond stability resulted in a higher percentage of NPs detaching from BPs 2 and 3, and significant detachment was now seen from BP4. Detachment was even observed from BP 6 for $k_r^0 = 10^{-3} \text{ s}^{-1}$. Detachment fits for each BP category can be found for both one (eq 5) and two sub-components (eq 8) in the Supplementary Information (see Supplementary Information, Fig. S4). Combined fits using the heterogeneous population and the empirical detachment models are shown in Figs. 4E-H. Even though detachment was now higher in magnitude with contributions from more BPs, the two component BP model still matched the NAD simulation data very well. Detachment rate constants ($k_{D,i}$) and relative numbers (α_i) for sub-component 1 of each BP are listed in Table 1. The largest differences relative to the base case were again related to $k_{D,1}$, which increased progressively with both γ and k_r^0 due to elevated $k_{r,1,1}$ (see Supplementary

Information, Fig. S1). Differences in $k_{D,2}$ from the base case were modest, but α_2 increased substantially. Both $k_{D,i}$ and α_i values continued to decrease with BP, but only modestly, indicating that single bond stability had less of an effect at high valency.

Estimating Detachment Rates for all Sub-Populations

To obtain detachment rates for the non-detaching BP sub-components, we utilized bonding information from the simulations. First, we sub-categorized NPs within each BP (i) based on instantaneous bond number (j), designated as bond number state $S_{i,j}$. We then used a system of ordinary differential equations (eq 11) to determine all bond formation ($k_{f,i,j}$) and rupture ($k_{r,i,j}$) rates. To simplify the solutions, we used exact values for $k_{r,1,1}$ (3.8 s^{-1}) and k_{diff} (66 s^{-1}) that were determined from single bond NAD simulations, and initial estimates for all other bond transition rates determined from pause times observed during the full multivalent NAD simulations (see Supplementary Information Methods for detailed information, and Table S3). Bond number fitting results for the base case (medium antibody and ICAM-1 density, $\gamma = 0.274 \text{ nm}$, $k_r^0 = 1.1 \times 10^{-4} \text{ s}^{-1}$) using two sub-components are presented in Fig. 5A-C, and matched the NAD simulation data well for all BPs. State transitions rates ($k_{f,i,j}$ and $k_{r,i,j}$) and the relative number of NPs in the lower energy sub-component for formation and rupture ($P_{f,i,j}$ and $P_{r,i,j}$) are listed in the Supplementary Information, Table S5. We then used the results in Table 3 to reconstruct NP detachment curves for each BP (Fig. 5D) and the entire population (Fig. 5E), which closely matched the NAD simulation data. Results were similar for the other eight parameter conditions (see Supplementary Information, Fig. S6 and Table S4). As expected, fitting results using one sub-component (eq 10) did not capture key feature of the data (see Supplementary Information, Fig. S4).

Next we used the microscopic bond transition rates ($k_{r,i,j}$, $k_{f,i,j}$, k_{diff}) to estimate a macroscopic NP detachment rate ($k_{D,i}$) based on the mean first passage time. The first passage

time ($T_{i,j}$), or time for detachment to occur, was calculated using the transition matrix (\mathbf{K}) and the transition rates listed in the Supplementary Information, Table S5, as described by eq 12.

Interestingly, we observed that first passage times were similar for all bond states within the BPs, and therefore we could simply average $T_{i,j}$ over state j to obtain $k^{(M)}_{D,i}$, as described by eq 13. Values for $k^{(M)}_{D,i}$ are listed in Table 3.

Detachment rate constants were determined for all BP categories and sub-components by again fitting the NAD simulation data using the population heterogeneity detachment model, but now using $k^{(M)}_{D,i}$ as an additional constraint, as shown in eq 14. Full population fits are shown in the Supplementary Information (see Supplementary Information, Fig. S8), and in general matched the simulation data in a similar manner to the initial results in Figs. 2-4. The lone exception was the base case, as the heterogeneous population model predicted more NPs would detach than was actually observed in the NAD simulation. Inspection of the profile in Fig. S8 indicated that detachment abruptly stopped after 5 seconds, which was likely due to a sampling issue since this condition had very low detachment numbers. Final detachment rates ($k_{D,i}$) and sub-component weights (α_i) are listed in Table 4 for all 9 parameter cases. Three of the cases now had two sub-components within BP1. However, α_i values were low (<10%) for most BPs >2, indicating that one of the sub-components was dominant.

Relating the Population Heterogeneity and Empirical Detachment Models

Finally, we sought to relate the new heterogeneous population detachment model and our original empirical detachment model with time-dependent behavior. Therefore, we performed a survival analysis to derive a net detachment rate using the individual BP detachment rates ($k_{D,i}$) and weights (α_i). For simplicity, we again assumed that two sub-components were present for each BP, allowing us to use the results in Table 1. We then defined a hazard function (H) to characterize an instantaneous detachment rate and NP survival

probability (\tilde{B}), as described in eq 17. The hazard function contained magnitude ($1/\tilde{\tau}$) and time-dependent (logistic decay $1/(1+e^{t/\tilde{\tau}})$) elements, similar to our original empirical detachment rate (eq 2). However, the empirical detachment rate scaled with a power law, $1/t^\beta$, and thus we could not compare the two models directly. Instead, we evaluated at specific time points, the time to reach multivalent bonding (t_{ref}) and an arbitrary later time (t_{max}). At t_{ref} , the time-dependent element of the empirical model vanished, allowing k_D^0 to be expressed explicitly in terms of parameters $\tilde{\tau}$ and $\tilde{\rho}$ (eq 20). At t_{max} , we solved explicitly for β , resulting in eq 21. Values for parameters $\tilde{\tau}$ and $\tilde{\rho}$, determined using eq 17 and data listed in Table 1, are listed in Table 2. Also included are k_D^0 and β values determined using eqs 20 and 21, as well as the empirical detachment model using eq 2. The respective k_D^0 values for the two models were remarkably similar, varying by at most 10%. Before we could evaluate β , we still needed to select a specific value for t_{max} . We anecdotally observed that the two models matched for most of the 9 parameter cases at $t_{max} = 5.5$ s. We then attempted to find the optimal value of t_{max} for matching β , which resulted in values ranging from 4 s for the clustered dimer to 12 s for $k_r^0 = 10^{-3} \text{ s}^{-1}$. Interestingly, these optimized t_{max} values were all approximately 3-fold greater than $\tilde{\tau}$. Values for k_D^0 ranged from 0.03 s^{-1} for the base case up to 0.18 s^{-1} for the clustered dimer. We note that k_D^0 was relatively low for $k_r^0 = 10^{-3} \text{ s}^{-1}$ even though it had the highest level of detachment, which was likely due to the strong influence of $\tilde{\tau}$. Values for β ranged from 0.45 for $k_r^0 = 10^{-3} \text{ s}^{-1}$ to 0.81 for the clustered dimer, and we observed a strong correlation with $1/\tilde{\tau}$.

Discussion

The goal of this work was to create a simple methodology for determining multiple detachment rates from nanoparticle populations that display heterogeneous bond numbers. The results could then be combined to reconstruct the empirically-observed behavior of the population. A critical aspect was the categorization criteria, which we defined as the BP and for

which we selected to use mode bond number. While this approach was generally successful, the need to utilize two sub-components to accurately fit detachment data indicated that significant bonding heterogeneity was still present even within BP sub-categories. This suggests that NPs tending to possess the same number of bonds can still display significantly different adhesion properties. Allowing for two sub-components provided a means to distinguish between relatively faster and slower detachment rates, or lower and higher bond energies. We believe that these sub-components likely arose from a physical mechanism with respect to the way in which adhesion molecules and/or bonds were distributed within the contact zone. For example, certain bond configurations may lead to higher levels of strain on one or more neighboring bonds, accelerating rupture. Alternatively, the presence of more unbound receptors or ligands could drive bond re-formation after a rupture event. We would expect that a configuration-based mechanism would be most prominent at lower BPs, where variation in adhesion molecule/bond distribution would be highest. This can in fact be seen in Tables 1, 3, and 4, as relative number of the fast-detaching sub-component (α_i or $P_{f,i}$, $P_{r,i}$) was highest for BP2, and then decreased with valency.

Using the hidden sub-component interpretation, we fit NAD simulation detachment data for each BP category using eq 7. However, it was clear that there was not enough information to characterize the slower detaching sub-component. Therefore, we simplified the fitting process by assuming that the slower detaching sub-component did not detach at all ($k_{D,i}^{(2)} = 0$). It should be noted that this assumption is only valid over the time frame observed, as all NPs should possess non-zero $k_{D,i}$ values. Since direct information about the slow detaching sub-populations could not be obtained from NP detachment (macroscopic) data, we turned to the bonding (microscopic) data. Using a system of ordinary differential equations (eq 11), we determined bond state transition (forward and reverse) rate values for each BP. We then used the bond transition rates and mean first passage time (eqs 12 and 13) to estimate a single macroscopic NP detachment rate ($k_{D,i}^{(M)}$) that corresponded to both sub-components. This was a result of our

decision to allow the sub-components to interact, such that a NP could crossover between at any time. We felt that this interpretation was more realistic than fully separating the sub-components, as NP rotation and translation could reveal new adhesion molecule configurations within the contact zone. After performing the fitting again, now using $k_{D,i}^{(M)}$ as an additional constraint (eq 14), we obtain results that are very similar during the observed time (see Supplementary Information, Fig. S9). However, the initial fits would predict that no more NPs would detach, which clearly is not accurate. Thus, the final fits with both macroscopic and microscopic consistency provide superior predictions of long-term detachment behavior. This could be important because NAD simulations are computationally expensive, requiring days of real time to simulate seconds of adhesion data.

Upon inspection of the final detachment rates ($k_{D,i}$) and sub-component weights (α_i) listed in Table 4, we conclude that most BPs were dominated by a single population of NPs. If two sub-components were present, one tended to be at a low percentage (<10%), which was likely linked to incorrect BP identification or a random event. For example, case 2 (low antibody density) had 3% of the BP1 population with an extremely fast detachment rate that was probably random, while 2% of the BP2 population had a fast detachment rate that was more consistent with BP1. As for detachment rates, we conclude that values were similar for BP1 across cases 1-5, which is reasonable since bond properties were the same and valency effects should have been captured by BP classification. The detachment rate for cases 1-3 were all $\sim 0.65 \text{ s}^{-1}$, which is 6-fold slower than the single bond rupture rate ($k_{r,1,1} = 3.8 \text{ s}^{-1}$, see Supplementary Information, Fig. S1) due to the ability to rebind at rate $k_{f,1,1}$. We note that even with rebinding, NP detachment rate was still 6000-fold higher than the unstressed off-rate for the antibody/ICAM-1 bond ($k_r^0 = 1.1 \times 10^{-4} \text{ s}^{-1}$). This was due to an entropic penalty that accompanies the tethering of a NP's Brownian motion, as we and others have previously discussed.^{17,27} When ICAM-1 was clustered (cases 4 and 5), detachment rate increased to $\sim 0.95 \text{ s}^{-1}$, likely due to lower rebinding rate. As expected, detachment rates for BPs 2 and 3 decreased successively to

~ 0.01 and $\sim 0.002 \text{ s}^{-1}$, respectively. Thus, NP stability improved by ~ 600 - 900 -fold between 1 to 2 bonds, but only an additional 5-fold between 2 to 3 bonds. For cases 6-7 in which individual bonds were destabilized by increasing γ or k_r^0 , detachment rates increased for all BPs in a dose-dependent manner relative to the respective single bond rupture rate ($k_{r,1,1}$, see Supplementary Information, Fig. S1).

Our final goal was to relate the parameters of the heterogeneous population and empirical detachment models. We first performed a survival analysis to estimate an instantaneous detachment rate for the full population (eq 16), which varied with time following the logistic decay function $1/(1+e^{t/\tilde{\tau}})$. The empirical detachment model k_D was based on the simple power law function $1/t^\beta$, as given by (eq 2). By evaluating both detachment models at two key time points, we then developed relationships between the empirical model parameters (k_D^0 and β) and the population heterogeneity parameters ($w_i, k_{D,i}, \alpha_i$), as shown in eqs 20 and 21. At t_{ref} , the exponential term reduced to ~ 1 for all parameter cases, leaving two scaling factors: $1/\tilde{\tau}$ and $1/(1+\tilde{p}/(1-\tilde{p}))$. In the absence of a non-detaching sub-component, the term $\tilde{p}/(1-\tilde{p})$ would reduce to 0 and k_D^0 would simply equal to $1/\tilde{\tau}$. As \tilde{p} increases, k_D^0 also increases because k_D is essentially decaying to a larger non-zero value. From the population perspective, $1/\tilde{\tau}$ can be thought of as a characteristic rate at which the population k_D stabilizes to its long-term value, which is non-zero because of \tilde{p} . To assess β , we defined k_D in terms of an arbitrary time point t_{max} , and discovered that the two detachment models matched for $t_{max} \sim 3\tilde{\tau}$. While we do not know the reason for this specific relationship, it does make intuitive sense that β should depend on $\tilde{\tau}$, as both dictate how long it will take for the detachment rate of the full population (k_D) to stabilize. While $\tilde{\tau}$ does appear within the numerator of eq 21, these terms reduced to constants for all cases studied in this work. Instead, β was strongly dependent on $\tilde{\tau}$ through an indirect connection to t_{max} in the denominator. Ultimately, we found that eqs 20 and 21 were remarkably accurate in reproducing empirical model parameters (Table 2). This implies that despite the

very different time-functions underlying the models, both share the same basic assumption that the NP population contained sub-populations that essentially do not detach during the time-scale observed. Most importantly, these findings suggest that it may be possible to use empirical fits of experimental data, which are simple and straightforward, to determine population distributions that can otherwise only be determined using computationally intensive NAD simulations. This would involve the empirical detachment model being used to estimate the relative number of NPs in the non-detaching sub-population (\tilde{p}) by means of k_D^0 and β . Detachment information for the remaining NPs would also be available from $\tilde{\tau}$.

In future work, we will continue to develop and apply the methods developed in this work to quantify multivalent detachment rates from experimental binding data exhibiting significant population heterogeneity, as evidenced by non-first order detachment kinetics with apparent time-dependency. At the present time, NAD simulations must first be used to determine BP distributions for the population. However, we are highly interested in directly analyzing naïve experimental binding data by leveraging the empirical detachment model. Substantial work will be needed to achieve this goal possible, but doing so would greatly expedite the analysis of multivalent NP adhesion data, and in general make the work far more accessible to other researchers in the field. Finally, we plan to study the effect of population heterogeneity on NP attachment rate (k_A), which is needed to determine the thermodynamic energy, or avidity ($k_A/k_{D,i}$). We anticipate that k_A will be less sensitive to BP since it only accounts for the first bond, however attachment may be favored to regions of the substrate with higher than average adhesion molecule density, which would in turn result in a higher ultimate BP. This could lead a secondary selection mechanism driving NPs to higher BP and overall stability, which will be studied in future work.

Acknowledgements

This work was supported in part by the National Science Foundation under Award Number 1539114. Any opinions, findings, and conclusions or recommendations expressed in this material are those of the authors and do not necessarily reflect the views of the National Science Foundation.

Supplementary Information

Methods describing single tether simulations, estimation of bond transition rates using simulation pause time fits, and development of the transition matrix. Tables for population heterogeneity model parameters for single component fits and two component fits using 2 and 3 degrees of freedom, simulation pause time fitting results, and final bond transition rates. Figures for bond transition rate model fitting, population heterogeneity model fits for two components using 2 and 3 degrees of freedom, individual BP detachment fits for cases 2-9, bond transition rate modeling using one component, bond transition rate modeling for the cases 2-9, and final population heterogeneity model fitting results and predictions.

Table 1. BP model parameters for two component fits assuming one does not detach.

Case	$k_{D,1}$ (s^{-1})	α_1	$k_{D,2}$ (s^{-1})	α_2	$k_{D,3}$ (s^{-1})	α_3	$k_{D,4}$ (s^{-1})	α_4	$k_{D,5}$ (s^{-1})	α_5	$k_{D,6}$ (s^{-1})	α_6
1. Base	0.57	1	0.19	0.30	0.01	0.05						
2. Low Antibody	3.17	1	0.06	0.42	0.03	0.12						
3. Low ICAM-1	0.57	1	0.06	0.33								
4. ICAM-1 dimer	0.81	1	0.08	0.23	0.05	0.08						
5. Clustered dimer	0.82	1	0.07	0.20								
6. $\gamma = 0.29$ nm	2.18	1	0.10	0.55	0.02	0.08						
7. $\gamma = 0.3$ nm	8.48	1	0.15	0.75	0.09	0.17	0.08	0.08	0.075	0.04		
8. $k_r^0 = 5 \times 10^{-4} s^{-1}$	7.10	1	0.10	0.55	0.07	0.15	0.05	0.08				
9. $k_r^0 = 1 \times 10^{-3} s^{-1}$	18.22	1	0.20	0.67	0.05	0.40	0.05	0.10	0.04	0.12	0.04	0.12

Table 2. Correlation between empirical and BP model parameters.

Case	Empirical		BP Model				
	k_D^0 (s^{-1})	β	\tilde{p}	\tilde{t} (s)	k_D^0 (s^{-1})	β	t_{max} (s)
1. Base	0.03	0.73	0.94	1.8	0.03	0.72	5.5
2. Low Antibody	0.04	0.55	0.87	2.1	0.05	0.54	6.5
3. Low ICAM-1	0.12	0.67	0.77	2.7	0.10	0.66	6.5
4. ICAM-1 dimer	0.15	0.73	0.77	1.7	0.13	0.75	5.5
5. Clustered dimer	0.19	0.82	0.74	1.2	0.21	0.81	4.0
6. $\gamma = 0.29$ nm	0.05	0.69	0.88	1.9	0.06	0.66	5.5
7. $\gamma = 0.3$ nm	0.14	0.65	0.73	1.9	0.14	0.64	5.5
8. $k_r^0 = 5 \times 10^{-4} s^{-1}$	0.09	0.67	0.82	1.9	0.09	0.68	5.5
9. $k_r^0 = 1 \times 10^{-3} s^{-1}$	0.08	0.45	0.65	4.8	0.07	0.44	12.0

Table 3. Mean first passage time calculations.

Case	$k^{(M)}_{D,i} (S^{-1})$					
	BP 1	BP 2	BP 3	BP 4	BP 5	BP 6
1. Base	0.70	0.06	4.6×10^{-6}			
2. Low Antibody	3.30	0.01	2.4×10^{-3}			
3. Low ICAM-1	0.62	0.01				
4. ICAM-1 dimer	0.93	8.5×10^{-3}	2.3×10^{-3}			
5. Clustered dimer	0.96	7.2×10^{-3}				
6. $\gamma = 0.29$ nm	3.57	0.04	0.01	2.1×10^{-3}		
7. $\gamma = 0.3$ nm	5.25	0.03	5×10^{-3}	1.6×10^{-3}	7.5×10^{-8}	
8. $k_r^0 = 5 \times 10^{-4} s^{-1}$	5.12	0.05	7.3×10^{-3}	2.7×10^{-3}		
9. $k_r^0 = 1 \times 10^{-3} s^{-1}$	22.75	0.02	3.8×10^{-7}	1.6×10^{-4}	7.3×10^{-4}	6×10^{-5}

Table 4. Final fitting parameters using detachment fitting and mean first passage time criteria.

*See separate file

Figure 1. Detachment for NP populations displaying heterogeneous bonding. The initial population contains NPs with different bonding ability, or bond potential (BP), as distinguished by color. BP is generally related to bond valency, and for this work we used mode bond number. Over time, NPs in each BP sub-population progressively detach at an approximately constant rate ($k_{D,i}$), predominantly from BP 1 and then, on average, progressing through higher BPs. For clarity, the schematic shows BP sub-populations detaching in a deterministic and sequential manner, whereas in reality the process would be stochastic. From the perspective of the overall population, it appears that detachment rate (k_D) decreases over time.

Figure 2. Population heterogeneity model analysis of the base case (medium antibody and ICAM-1 density, $\gamma = 0.274$ nm, $k_r^0 = 1.1 \times 10^{-4}$ s $^{-1}$). (A) Histogram showing the NP distribution across BPs 1-6. The number of NPs that detached during 30 s simulations is shown in red. (B) Individual detachment profiles for (i) BP 1, (ii) BP 2, and (iii) BP 3, along with fits performed using one and two hidden sub-components. (C) Detachment profile for the full NP population and fits performed using the population heterogeneity model with one and two sub-components, as well as the empirical model.

Figure 3. Analysis of cases 2-5. Base case parameters were modified by (A,E) decreasing antibody density, (B,F) decreasing ICAM-1 density, (C,G) arranging ICAM-1 as dimers, and (D,H) clustering ICAM-1 dimers. (A-D) Histograms showing NP distributions across BPs 1-6. The number of NPs that detached during 30 s simulations is shown in red. (E-H) Full population detachment profiles and fits performed using the population heterogeneity model with one and two sub-components, as well as the empirical model.

Figure 4. Analysis of cases 6-9. Bond properties for the base case were modified to (A,E) $\gamma = 0.29$ nm, (B,F) $\gamma = 0.3$ nm, (C,G) $k_r^0 = 5 \times 10^{-4} \text{ s}^{-1}$, and (D,H) $k_r^0 = 10^{-3} \text{ s}^{-1}$. (A-D) Histograms showing NP distributions across BPs 1-6. The number of NPs that detached during 30 s simulations is shown in red. (E-H) Full population detachment profiles and fits performed using the population heterogeneity model with one and two sub-components, as well as the empirical model.

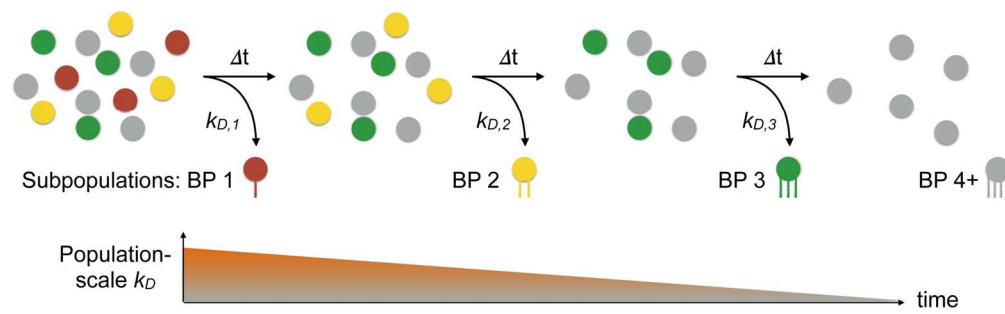
Figure 5. Bond transition rate modeling for the base case (medium antibody and ICAM-1 density, $\gamma = 0.274$ nm, $k_r^0 = 1.1 \times 10^{-4} \text{ s}^{-1}$) using two sub-components. (A-C) Simulation profiles and fits for NPs within each bond number state for (A) BP 1, (B) BP 2, and (C) BP 3. The detachment profile is also overlaid in black for each BP category. (D,E) Detachment curves from the simulation data and model fits for (D) each BP category shown relative to the initial distribution and (E) the full population.

References

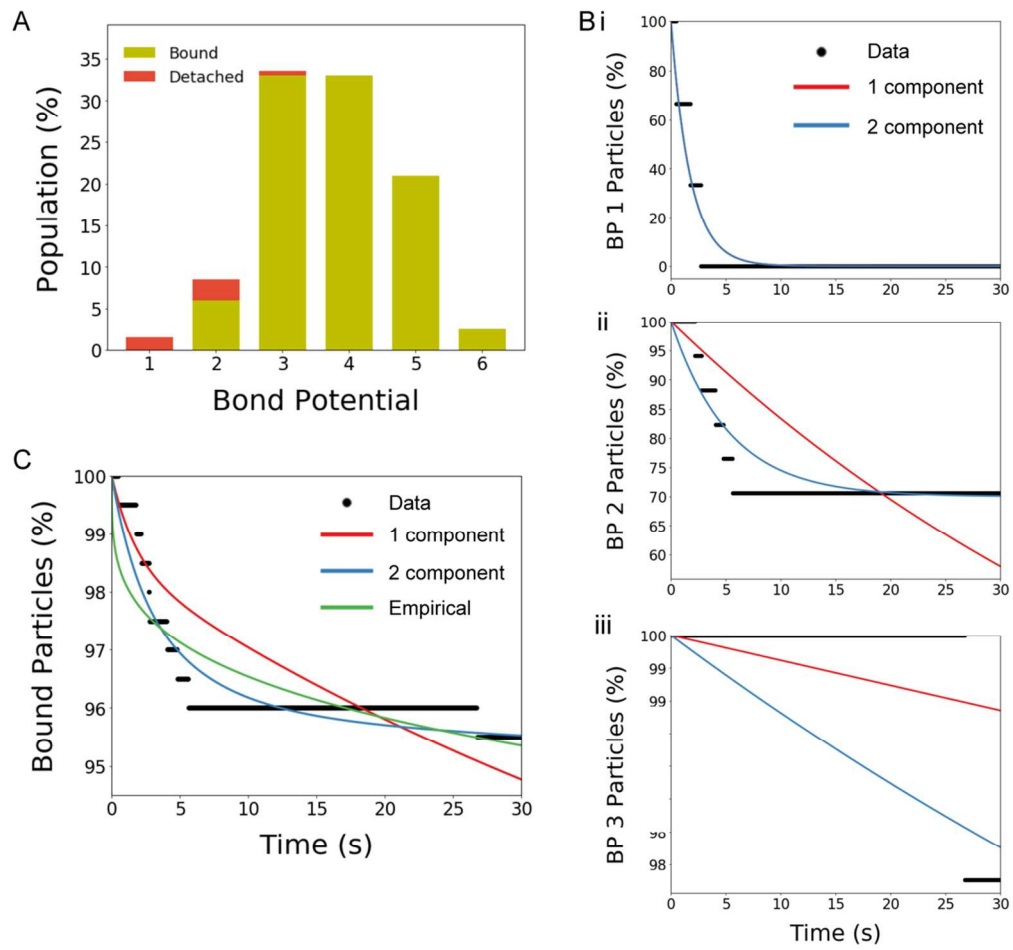
1. S. Muro, T. Dziubla, W. Qiu, J. Leferovich, X. Cui, E. Berk and V. R. Muzykantov, *J. Pharmacol. Exp. Ther.*, 2006, **317**, 1161-9.
2. S. Hong, P. R. Leroueil, I. J. Majoros, B. G. Orr, J. R. J. Baker and M. M. Banaszak Holl, *Chem. Biol.*, 2007, **14**, 107-15.
3. J. B. Haun and D. A. Hammer, *Langmuir*, 2008, **24**, 8821-32.
4. W. Jiang, B. Y. Kim, J. T. Rutka and W. C. Chan, *Nat. Nanotechnol.*, 2008, **3**, 145-50.
5. J. B. Haun, G. P. Robbins and D. A. Hammer, *J. Adhesion*, 2010, **86**, 131-59.
6. C. Tassa, J. L. Duffner, T. A. Lewis, R. Weissleder, S. L. Schreiber, A. N. Koehler and S. Y. Shaw, *Bioconjug. Chem.*, 2010, **21**, 14-9.
7. J. Wang, S. Tian, R. A. Petros, M. E. Napier and J. M. Desimone, *J. Am. Chem. Soc.*, 2010, **132**, 11306-13.
8. J. B. Haun, L. R. Pepper, E. T. Boder and D. A. Hammer, *Langmuir*, 2011, **27**, 13701-12.
9. B. J. Zern, A. M. Chacko, J. Liu, C. F. Greineder, E. R. Blankemeyer, R. Radhakrishnan and V. Muzykantov, *ACS Nano*, 2013, **7**, 2461-9.
10. D. T. Wiley, P. Webster, A. Gale and M. E. Davis, *Proc. Natl. Acad. Sci. U.S.A.*, 2013, **110**, 8662-7.
11. P. I. Kitov and D. R. Bundle, *J. Am. Chem. Soc.*, 2003, **125**, 16271-84.
12. J. Huskens, A. Mulder, T. Auletta, C. A. Nijhuis, M. J. Ludden and D. N. Reinhoudt, *J. Am. Chem. Soc.*, 2004, **126**, 6784-97.
13. D. J. Diestler and E. W. Knapp, *Phys. Rev. Lett.*, 2008, **100**, 178101.
14. S. Wang and E. E. Dormidontova, *Biomacromolecules*, 2010, **11**, 1785-95.
15. S. Wang and E. E. Dormidontova, *Soft Matter*, 2011, **7**, 4435-45.
16. S. Wang and E. E. Dormidontova, *Phys. Rev. Lett.*, 2012, **109**, 238102.
17. M. Wang, S. R. Ravindranath, M. K. Rahim, E. L. Botvinick and J. B. Haun, *Langmuir*, 2016, **32**, 13124-36.

18. D. A. Hammer and S. M. Apte, *Biophys. J.*, 1992, **63**, 35-57.
19. N. A. Mody and M. R. King, *Biophys. J.*, 2008, **95**, 2539-55.
20. N. A. Mody and M. R. King, *Biophys. J.*, 2008, **95**, 2556-74.
21. T. J. English and D. A. Hammer, *Biophys. J.*, 2004, **86**, 3359-72.
22. T. J. English and D. A. Hammer, *Biophys. J.*, 2005, **88**, 1666-75.
23. A. D. Trister and D. A. Hammer, *Biophys. J.*, 2008, **95**, 40-53.
24. D. Oh, M. Ogiue-Ikeda, J. A. Jadwin, K. Machida, B. J. Mayer and J. Yu, *Proc. Natl. Acad. Sci. U.S.A.*, 2012, **109**, 14024-9.
25. S. M. Ross, *Introduction to Probability Models*, Academic Press, 2014.
26. T. Chou and M. R. D'Orsogna, *First-passage phenomena and their applications*, World Scientific, 2014.
27. J. Liu, G. E. Weller, B. Zern, P. S. Ayyaswamy, D. M. Eckmann, V. R. Muzykantov and R. Radhakrishnan, *Proc. Natl. Acad. Sci. U.S.A.*, 2010, **107**, 16530-5.

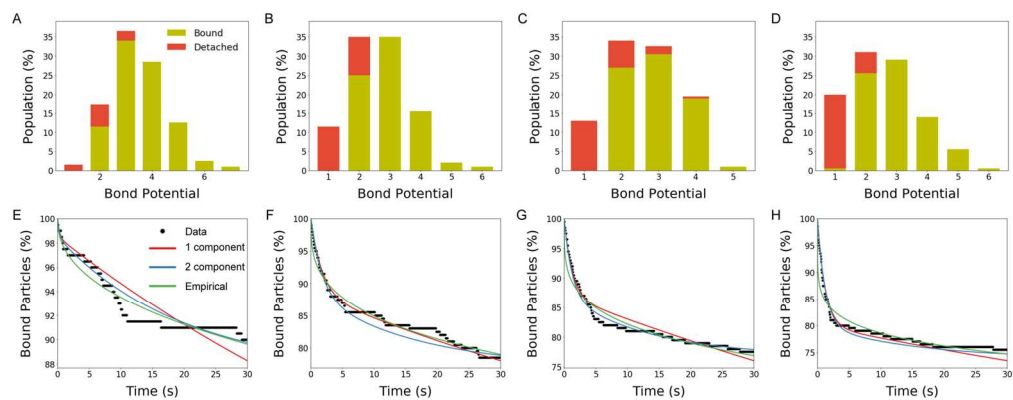
Case	$k^{(1)}_{D,i} (\text{s}^{-1}), k^{(2)}_{D,i} (\text{s}^{-1}), \alpha_i$																	
	BP 1			BP 2			BP 3			BP 4			BP 5			BP 6		
1. Base	0.70		1	0.06		1	1.5×10^{-4}		1									
2. Low Antibody	3.30	0.63	0.03	0.53	0.01	0.02	2.4×10^{-3}		1									
3. Low ICAM-1	0.62		1	0.28	0.01	0.12												
4. ICAM-1 dimer	0.93		1	0.46	8.5×10^{-3}	0.05	2.3×10^{-3}		1									
5. Clustered dimer	0.96	0.25	0.95	2.40	7.2×10^{-3}	0.02												
6. $\gamma = 0.29$ nm	2.20		1	0.04		1	0.01		1	2.1×10^{-3}		1						
7. $\gamma = 0.3$ nm	37.40	5.12	0.63	0.23	0.03	0.58	5.0×10^{-3}		1	0.20	1.6×10^{-3}	0.04	7.5×10^{-8}		1			
8. $k_r^0 = 5 \times 10^{-4} \text{ s}^{-1}$	7.10		1	0.05		1	7.3×10^{-3}		1	2.7×10^{-3}		1						
9. $k_r^0 = 1 \times 10^{-3} \text{ s}^{-1}$	18.22		1	0.26	0.02	0.53	0.02	3.8×10^{-7}	0.64	0.14	1.6×10^{-4}	0.06	7.3×10^{-4}		1	0.02	6.0×10^{-5}	0.61



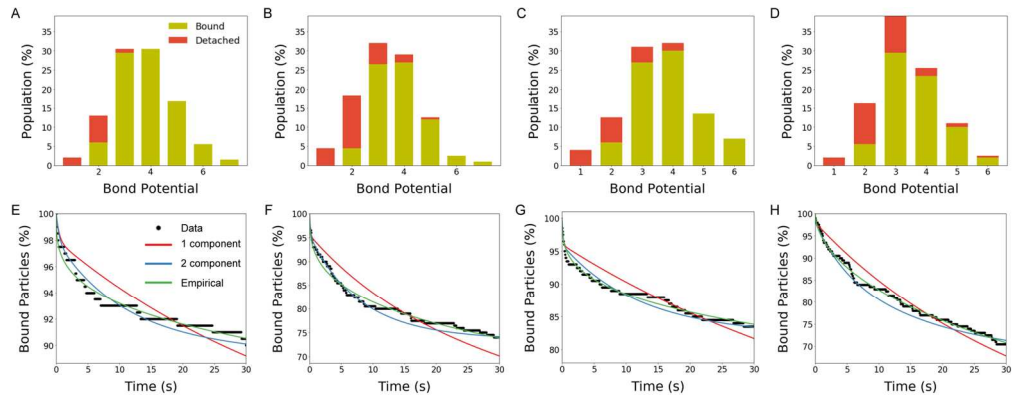
165x49mm (300 x 300 DPI)



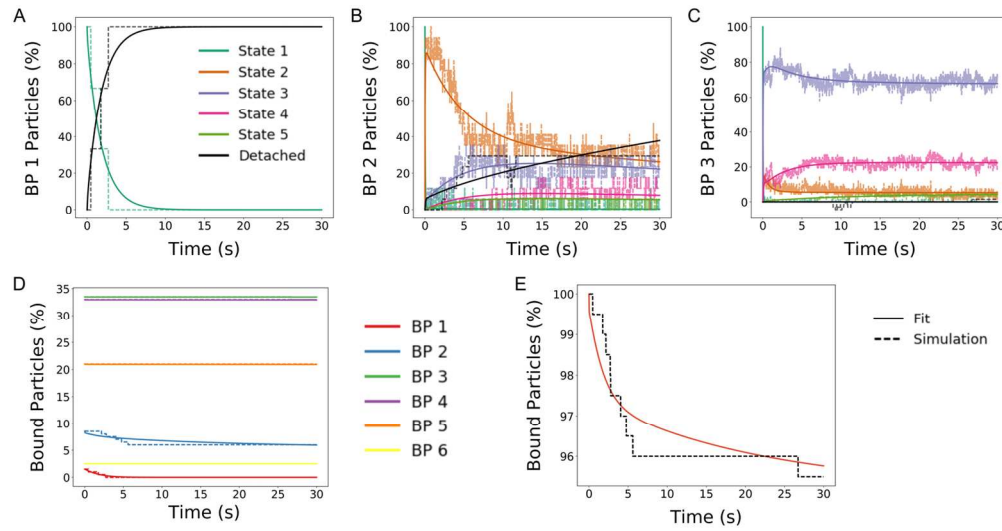
114x106mm (300 x 300 DPI)



165x63mm (300 x 300 DPI)



165x63mm (300 x 300 DPI)



139x72mm (300 x 300 DPI)

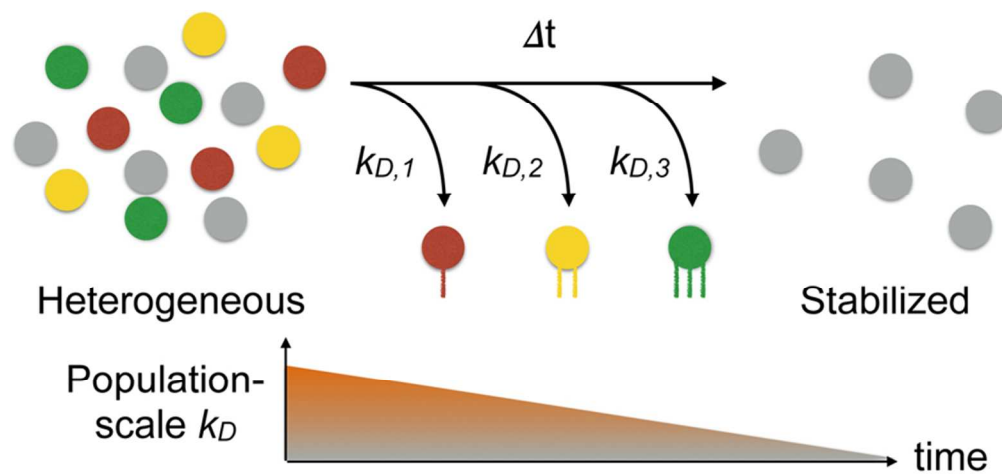


Table of content legend:

We present a methodology for isolating detachment rates from antibody-targeted nanoparticle populations with heterogeneous bond numbers

80x37mm (300 x 300 DPI)